

Structure and Morphology of Organic Semiconductor–Nanoparticle Hybrids Prepared by Soft Deposition

R. Banerjee,^{*,†} J. Novák,^{†,‡} C. Frank,[†] M. Girleanu,[§] O. Ersen,[§] M. Brinkmann,^{||} F. Anger,[†] C. Lorch,[†] J. Dieterle,[†] A. Gerlach,[†] J. Drnec,[⊥] S. Yu,^{#,○} and F. Schreiber[†]

[†]Universität Tübingen, Institut für Angewandte Physik, Auf der Morgenstelle 10, 72076 Tübingen, Germany

[‡]Central European Institute of Technology, Masaryk University, Kamenice 5, CZ-62500 Brno, Czech Republic

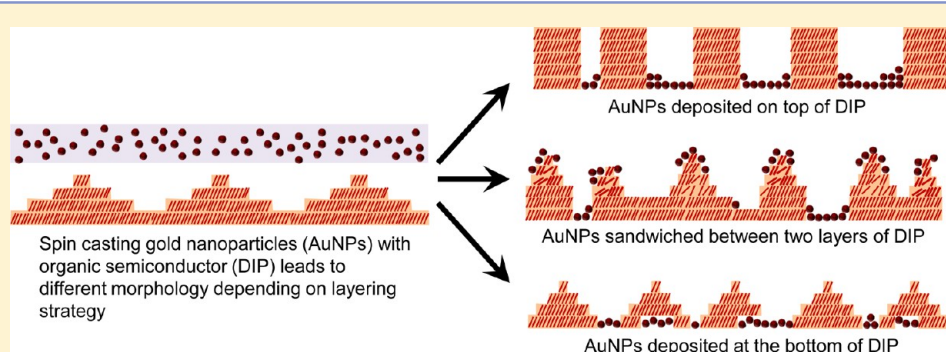
[§]Institut de Physique et Chimie des Matériaux de Strasbourg, UMR 7504 CNRS-UdS, 23 rue du Loess BP43, 67034 Strasbourg Cedex 2, France

^{||}Institut Charles Sadron, UPR 22 CNRS, 23 rue du Loess BP 84047, 67034 Strasbourg, France

[⊥]European Synchrotron Radiation Facility, 6 Rue Jules Horowitz, BP 220, 38043 Grenoble Cedex 9, France

[#]Deutsches Elektronen-Synchrotron (DESY), Notkestraße 85, 22607 Hamburg, Germany

[○]Department of Fiber and Polymer technology, Royal Institute of Technology, Teknikringen 56-58, SE-10044 Stockholm, Sweden



ABSTRACT: We present an extensive structural analysis of hybrid architectures prepared by the “soft” incorporation of gold nanoparticles (AuNPs) within an organic semiconductor matrix of diindenoperylene (DIP). Such “soft” or noninvasive deposition of nanoparticles within organic semiconducting host matrices not only minimizes the influence of the deposition process on the order and properties of the organic host molecules, but also offers additional control in the process of incorporation. The hybrid structures were characterized by X-ray scattering techniques including grazing incidence small angle X-ray scattering (GISAXS), grazing incidence X-ray diffraction (GIXD), X-ray reflectivity (XRR), and complemented by atomic force microscopy (AFM), photoluminescence (PL) spectroscopy, and transmission electron microscopy (TEM) measurements. We show that different strategies of incorporating the nanoparticles in the host matrix lead to drastically different structure and morphologies. Particularly remarkable is the morphological change observed in the matrix of DIP as well as the AuNPs due to the influence of organic solvents, as evidenced by TEM tomography measurements, which revealed the exact location of the AuNPs within the organic host. It is also demonstrated that AuNPs can be successfully used as tunable templates for the growth of the organic semiconductors with desired island sizes and distances.

INTRODUCTION

Small molecular organic semiconductors exhibit fascinating optoelectronic and structural properties which have led to widespread device applications like field-effect transistors, photodiodes, organic photovoltaics, and organic light emitting diodes.^{1–5} In some cases, combining organic semiconductors (OSCs) with metal nanoparticles (MNPs) leads to additional features, for example, by tailored optical absorption due to “antenna effects” and plasmonics.^{6–16}

Hybrid materials comprised of metal nanoparticles embedded within organic semiconductor matrices in different possible configurations open up new application perspectives in electronics and optoelectronics. The presence of MNPs in

solar cells can enhance their power conversion efficiency under certain circumstances.^{9,11,14,15} The application of optical antennas in photodetection and photovoltaics is very promising since the antenna increases the absorption cross-section (and, hence, the harvested light flux), thereby potentially reducing the required thicknesses of the active layers, while retaining the optical absorption.¹⁰ Metal nanostructures (Au and Ag in particular) are ideally suited to serve as optical antennas since they act as subwavelength scattering centers and, consequently,

Received: January 16, 2015

Revised: February 9, 2015

Published: February 9, 2015

couple with sunlight, exploiting the excited plasmonic near-field and surface plasmon-polariton modes.¹⁷ Memory effects in thin films of such hybrid materials have also been realized.^{18,19} For hybrid materials the controlled preparation is still a challenge since solution-based soft deposition of nanoparticles has to be made compatible with vacuum based OSC growth.

However, for any hybrid device structure incorporating MNPs for enhanced performance, the output will strongly depend on the size and spatial distribution of such MNPs within the host matrix which is not trivial to determine and often involves complementary usage of advanced characterization techniques.²⁰ A thorough understanding of their growth and structure is a prerequisite to the efficient implementation on a technological basis, since the morphology of OSCs has a strong impact on their charge carrier mobility and other physical properties.^{1,20–30} The basic understanding has largely remained on a qualitative level, since in most cases the film structure is not sufficiently well-defined due to complex structural phenomena such as phase coexistence, changes in the molecular conformation or orientation, and morphological transitions. Thus, there is the avid need to comprehend the different structural aspects of the hybrid structures like, for example, the growth and structural properties of the host organic films, the controlled ordering and density distribution of MNPs with a desired area coverage within the organic layers and their potential impact on the properties of the organic host.

Functionalized gold nanoparticles (AuNPs; see Figure 1: (a) for schematic representation and (c) for TEM measurements) have been studied extensively due to their remarkable electronic, optical and structural properties, due to which they have found widespread usage in many electronic and optoelectronic devices as well as applications to catalysis and biology.^{31–33} Unique properties of AuNPs are attributed to the confinement effect of charge carriers and the excitation of localized plasmons in an external field.³⁴ The resulting physical properties strongly depend on the particle size, shape, interparticle distance, nature of the protecting organic shell, and the local dielectric environment.^{33,35,36}

Diindenoperylene (DIP, $C_{32}H_{16}$), similar to pentacene, is a typical rod-like OSC (see Figure 1b for molecular structure) with ambipolar transport properties²⁷ and a high order of crystalline growth.³⁷ DIP exhibits very interesting structural,^{38–41} optical,⁴² and electronic properties,^{43–46} and the structure can be tuned by varying the growth parameters like temperature and growth rate. In combination with C_{60} , DIP has proven to be a model donor/acceptor system for the realization of OPVs^{21,23} and demonstrated kinetically limited thickness-dependent phase separation⁴⁷ on coevaporation. This proves to be a good choice for a host since most of the properties are well-known, and any change from the pristine characteristics would imply influence of the presence of a guest material.

In this paper, we show extensive structural characterization of hybrid structures synthesized by incorporation of AuNPs in a prototypical rod-like organic semiconductor DIP using “soft” (i.e., noninvasive) deposition techniques to obtain stable and controlled metal–organic interfaces. The AuNPs were strategically placed, respectively, on top, at the bottom and sandwiched within the organic DIP host matrix (see Figure 1d for schematics) and their concentration varied in the organic host. The structure and morphology of such hybrid systems have been investigated using X-ray reflectivity (XRR), grazing incidence small-angle X-ray scattering (GISAXS), grazing incidence X-ray diffraction (GIXD), atomic force microscopy

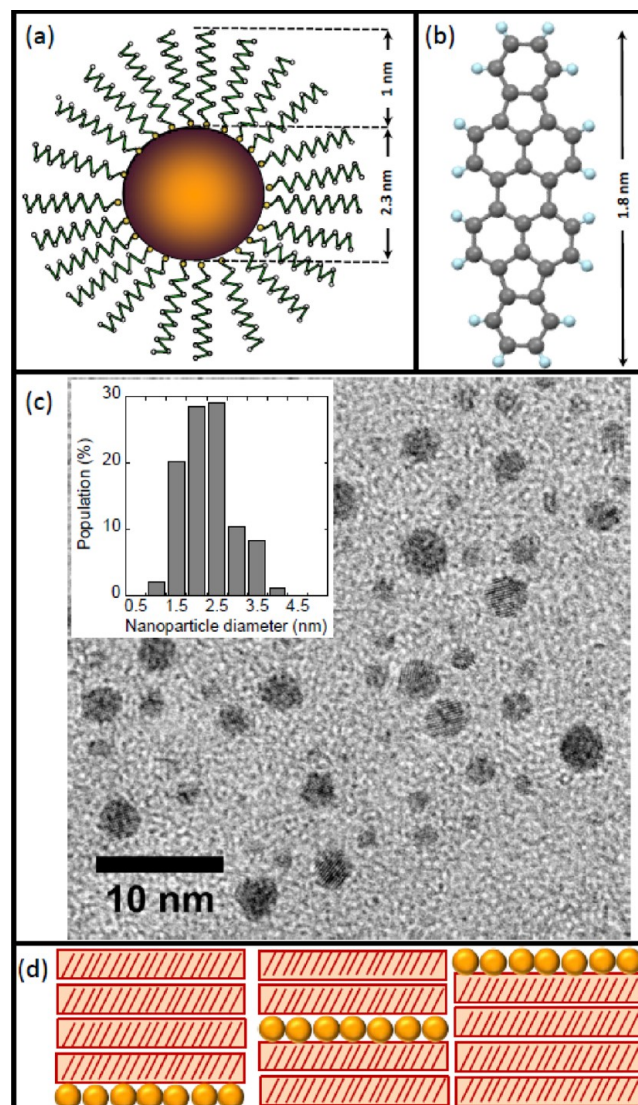


Figure 1. (a) Schematic representation of a dodecanethiol functionalized gold nanoparticle (AuNPs) and (b) molecular structure of diindenoperylene (DIP). (c) Bright field TEM image of the functionalized gold nanoparticles. Inset shows the size distribution of the metallic core of the nanoparticles with an average size of 2.3 ± 0.5 nm. (d) Sketches depicting the architecture of the AuNP–DIP hybrid structures, where the AuNPs were either placed on top, at the bottom, or sandwiched within the organic DIP host matrix. The concentration of the incorporated AuNPs was also varied to investigate the influence of larger density of the nanoparticles in the hybrids.

(AFM), and transmission electron microscopy (TEM) techniques. Photoluminescence (PL) measurements were also performed to test the variation in the PL yield of the weakly absorbing DIP in close vicinity of the AuNPs with different layering strategies. Differences in the PL yield were observed in the measurements on the DIP–AuNP hybrids with different layering strategies and were found to be strongly dependent on the precise location of the AuNPs within the organic matrix. The results provide new insights into the structural aspects of hybrid materials involving nanostructures.

EXPERIMENTAL SECTION

Gold nanoparticles functionalized with dodecanethiol ($\text{CH}_3(\text{CH}_2)_{11}\text{SH}$) were synthesized (Figure 1a) by using the

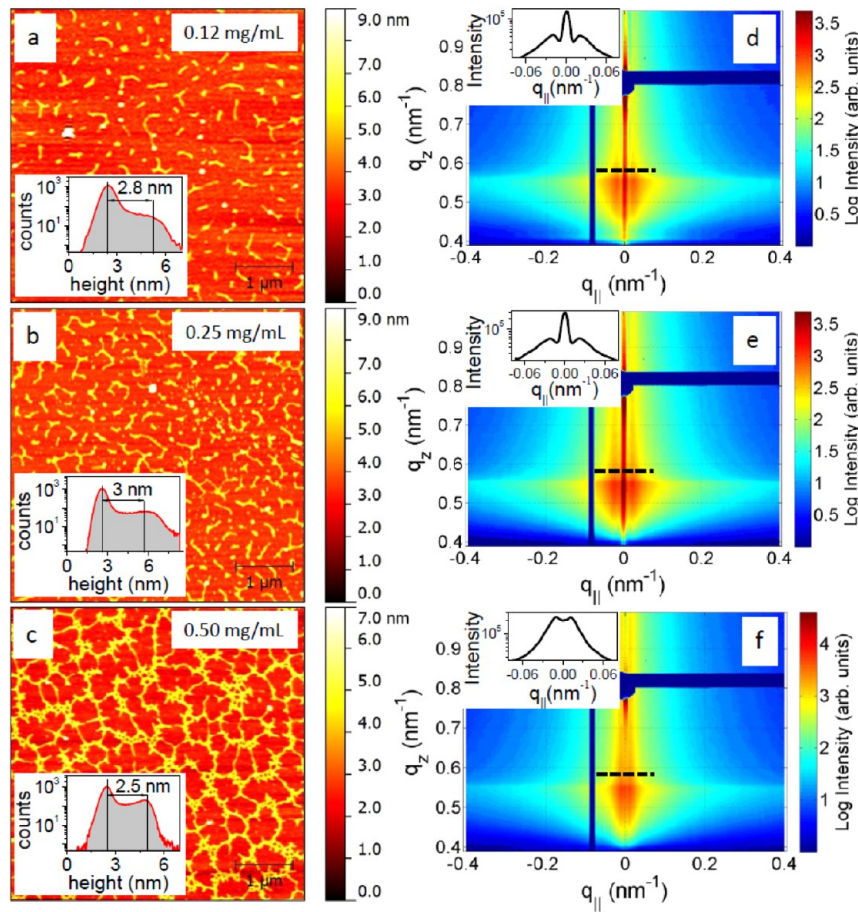


Figure 2. AFM images of the pure AuNPs, with different concentrations of (a) 0.12, (b) 0.25, and (c) 0.50 mg/mL in toluene, spin-coated on silicon substrate. The characteristic length scale of the pattern formed via drying mediated self-assembly depends on the concentration of the AuNPs. (d–f) Corresponding GISAXS data for the AuNPs which also show in-plane correlation lengths as evidenced by the two intense streaks on the GISAXS intensity contour on either side of $q_{||} = 0$ along the q_z direction. Inset shows the horizontal section extracted at $q_z = 0.57 \text{ nm}^{-1}$. The separation between the two side peaks is used to estimate the in-plane correlation length of the AuNP films. The length scales extracted using GISAXS matches with the ones estimated by AFM.

Brust method⁴⁸ of phase-transfer redox reaction.^{49,50} The nanoparticles dispersed in the toluene solution were rinsed in methanol to eliminate excess reagents and filtered out. Once dry, the nanoparticles were redispersed in a fixed quantity of toluene solution to obtain a desired concentration of the nanoparticles. Sublimation grade DIP (99.9% purity) was obtained from the Institut für PAH Forschung Greifenberg, Germany. DIP was deposited by organic molecular beam deposition (OMBD) technique at a growth rate of 2 Å/min at room temperature (25 °C) on silicon substrate with native oxide coating (~12 Å) at a base pressure <8 × 10⁻⁹ mbar. The substrate was thoroughly rinsed and cleaned using ethyl alcohol and acetone in an ultrasonic bath. The growth rate and final film thickness was monitored by a quartz crystal microbalance.

Three series of hybrid layers corresponding to different preparation protocols were prepared, each for three different AuNP concentrations. For the 1st series of samples, 20 μL of three different concentrations of AuNPs dispersed in toluene (0.12, 0.25, and 0.50 mg/mL) were deposited by spin-coating on the silicon substrate at 20 °C at a rotation speed of 1000 rpm for 1 min. After drying, 20 nm of DIP was deposited on top using OMBD technique (see left panel of Figure 1d for schematic illustration). For all the AuNP films prepared by spin-casting, although different concentrations of the AuNPs were used, the final thicknesses were only one monolayer (~2.5

nm). The hybrids thus fabricated have only the equivalent of a single monolayer of AuNPs incorporated in different layering strategies (i.e., different depths, particle density, and morphology) with respect to the DIP host matrices. We present only the representative data for one of the sample series where the AuNP concentration is 0.25 mg/mL. For the 2nd series of samples, the AuNP was sandwiched in between two 10 nm layers of DIP (middle panel of Figure 1d) and for the 3rd series of samples, 20 nm of DIP was already deposited on the silicon substrate and then the AuNP layer was spin-coated on top of it (right panel of Figure 1d). For convenience we henceforth refer to the different sample series as Au^{bot} , Au^{sand} , and Au^{top} for the AuNPs at the bottom of DIP, sandwiched between two layers of DIP and on top of DIP, respectively.

Transmission electron microscopy (TEM) was performed on a CM12 FEI microscope at 120 kV equipped with a megaview III CCD camera. For TEM analysis, the samples were coated with a carbon film in order to reduce the electron beam damage and the charging effects during the TEM analysis. Then, small drops of an aqueous poly(acrylic acid) (PAA) solution (25% in weight, Aldrich) were deposited on the samples and left for drying. The dried PAA drops were stripped off the substrate and deposited on distilled water to dissolve PAA and finally recovered on TEM copper grids. Electron tomography analysis was made with a JEOL 2100F transmission electron micro-

scope equipped with a field emission gun operating at 200 kV, a spherical aberration probe corrector and a GATAN Tridiem energy filter. Acquisitions of the tilt images series were performed using a high tilt sample holder from the GATAN Company. The irradiation damage was limited by using low electron doses and angles ranging from +62.5 to -62.5°, with projections taken every 2.5°. The contrast was improved by using an objective diaphragm of 40 μm in diameter. The acquisition of the 50 TEM tilt images series was achieved with a cooled CCD detector (2048 × 2048 pixels with a pixel size of 0.25 nm). The images were first roughly aligned using a cross-correlation algorithm. A refinement of this initial alignment and a precise determination of the tilt axis direction were then obtained using the IMOD software where the centers of several AuNPs from the analyzed group were used as fiducial markers.⁵¹ The volume reconstructions have been computed using an iterative approach consisting of a simultaneous algebraic reconstruction technique implemented using the TOMO3D software.⁵² Visualization and quantitative analysis of the final volumes were carried out using ImageJ software. TEM image of the pure AuNPs has been shown in Figure 1c. The average diameter of the metallic core of the nanoparticle was estimated to be 2.3 ± 0.5 nm (inset of Figure 1c).

GISAXS measurements were carried out at the P03 MiNaXS beamline^{53,54} in PETRA III at HASYLAB (Germany) on the samples kept in nitrogen atmosphere to reduce radiation damage. All measurements were performed at constant energy of 11.4 keV (corresponding to a wavelength of 1.0868 Å), using a Pilatus 1 M detector (981 × 1043 pixels). X-ray incidence angle (α_i) was 0.39°, and the sample to detector distance was about 5 m (evacuated flight path), providing not only very high resolution but also high signal-to-noise ratio.

XRR and GIXD were carried out at the ID03 beamline at the ESRF using a focused beam, the same sample environment and same energy using a Pilatus 300 K detector. The XRR is measured under specular conditions (incident angle (α_i) = exit angle (α_f)), where $q_z = (4\pi)/(\lambda) \sin \alpha_i$ is the out-of-plane and the only nonzero component of the wave vector (\mathbf{q}) and gives out-of-plane information. The GIXD, on the other hand, is measured along the in-plane angle (2θ) with a fixed grazing incidence angle of $\alpha_i = 0.1^\circ$ ($<\alpha_c$, the critical angle of DIP, which is $\sim 0.12^\circ$) and probes the in-plane component ($q_{||} = (4\pi)/(\lambda) \sin \theta$) of \mathbf{q} , which provides information on the in-plane crystallinity of the samples. Measurements were repeated for data reproducibility and radiation damage checks. The raw data was preprocessed and corrected for footprint and background contributions. AFM was measured using a JPK Nanowizard II instrument in tapping mode under ambient conditions and image processing and analysis were done by using the Gwyddion software.⁵⁵ PL spectra were acquired using a Horiba Jobin Yvon Labram HR 800 spectrometer with a CCD-1024 × 256-OPEN-3S9 as detector. Excitation for PL was performed using a frequency doubled Nd:YAG laser at 532 nm corresponding to an energy of 2.33 eV at a temperature of 20 °C.

RESULTS AND DISCUSSION

Grazing Incidence Small-Angle X-ray Scattering. The GISAXS technique probes the morphology and preferential ordering of nanostructures at the surface by typically utilizing an area detector. The 2D GISAXS profile provides information on the lateral correlation lengths as well as the sizes and shapes of nanostructures on the surface.^{56–58} The AFM and GISAXS

measurements (see Figure 2) were performed first on the thin films of pure AuNPs (with varying concentration) on silicon substrate. Pattern formation is observed in the AuNP films with characteristic pattern length scale which varies with the concentration of the AuNPs. The coverages estimated from the AFM images (Figure 2a–c) are 10, 25, and 40% for the AuNPs with concentration of 0.12, 0.25, and 0.50 mg/mL, respectively. The height distribution (see insets of Figure 2a–c) clearly suggests that the AuNP thickness is still one monolayer, that is, no second monolayer is formed, even for a coverage of 40%.

Pattern formation in AuNPs spin-coated on silicon has been studied extensively^{49,59–61} and is attributed to drying-mediated self-assembly of the nanoparticles. The pattern formation is achieved by the gradual evaporation of the solvent creating a dry area which keeps expanding as there is further evaporation of the solvent. The nanoparticles are thus dragged along the outer periphery of such voids similar to the “coffee-stain” effect⁶² observed in colloidal systems as a result of contact-line pinning and solvent evaporation. The nanoparticles are arrested as soon as they reach the boundary of another similar void or if all of the solvent evaporates. In either case, the dynamics stops and the nanoparticles are stranded forming patterns ranging from regular single to multilength scale cellular structure, worm-like structures, continuous labyrinthine to fractal structures, depending on the experimental conditions as well as the interplay of the nanoparticle–nanoparticle and the nanoparticle–solvent interaction.^{61,63} The AFM images clearly show that unless there is a high enough concentration of nanoparticles (e.g., 40% coverage, as seen in Figure 2c), the patterns are not formed completely and only an intermediate step toward patterning is realized (as evidenced in both Figure 2a and b) due to the lack of nanoparticles.

The in-plane length scale of the nanoparticles (distance of one cluster of nanoparticles to another) increases with the concentration as observed in the AFM images (Figure 2a–c) and is also corroborated by the evaluation of the GISAXS data shown in Figure 2d–f. The presence of distinct side peaks at particular $q_{||}$ values in the GISAXS profiles clearly indicates the presence of well-defined in-plane characteristic length scales on the surface. The length scales estimated from the horizontal line-scans of the GISAXS profiles (insets of Figure 2d–f) for the pure AuNP films are 267, 286, and 585 nm (with an error of $\leq 10\%$) for the nanoparticles with concentration of 0.12, 0.25, and 0.50 mg/mL, respectively. The in-plane correlation lengths of the nanoparticles are different for the different concentrations. For the lowest concentration of the AuNPs (i.e., 0.12 mg/mL), the nanoparticles do not form closed patterns so the correlation length corresponds to the distance between the end-points of the filamentary (worm-like) AuNP clusters and not the distance between two disconnected clustering sites. The correlation of the AuNP clusters (267 nm for $\text{AuNP}^{0.12}$) does not exist beyond this length scale. For a higher concentration of AuNPs (0.25 mg/mL), the correlation lengths is slightly larger (286 nm for the $\text{AuNP}^{0.25}$ compared to 267 nm for $\text{AuNP}^{0.12}$) because the number of AuNPs connected to such filaments increase, resulting in longer interconnected filamentary clusters. However, for the highest concentration (0.50 mg/mL) of the AuNPs ($\text{AuNP}^{0.50}$), closed patterned networks are formed whose correlation length is now given by the average distance between the connecting points or nodes (which now form the vertices of the polygonal networks), where the AuNPs have aggregated. The correlation

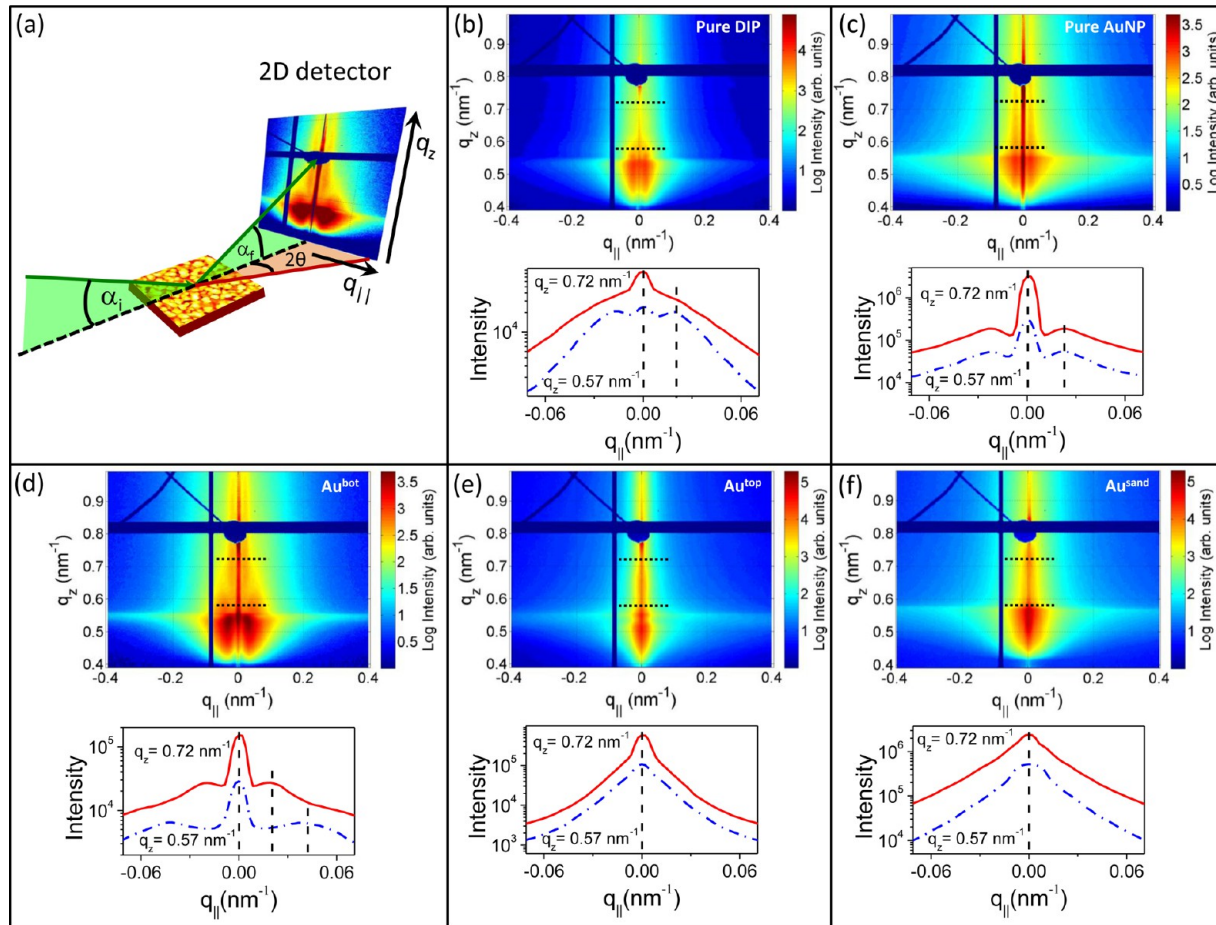


Figure 3. (a) Schematic of the GISAXS scattering geometry. (b, c) GISAXS images of the pure DIP and pure AuNP thin films, respectively. (d, e, f) GISAXS images of the hybrid structures with AuNP at the bottom (Au^{bot}), on top (Au^{top}), or sandwiched in-between the DIP layers (Au^{sand}), respectively. In both the pure and hybrid structures, the concentration of the AuNPs used was 0.25 mg/mL. Two horizontal line profiles (shown in the lower panel of the individual images) at two different q_z values of 0.57 and 0.72 nm^{-1} were extracted out of the GISAXS profiles to probe the variation of the in-plane correlation lengths as a function of different depths within the film.

length is now quite large (585 nm for $\text{AuNP}^{0.50}$) because the AuNP clusters are correlated over the entire pattern length scale. These length scales are in decent agreement with those observed from AFM measurements.

Figure 3 shows the GISAXS images (see Figure 3a for schematic representation) of the pure samples as well as the hybrid samples with layers of AuNPs embedded in different configurations in the DIP matrix. We observe distinct side peaks in the GISAXS measurements at different $q_{||}$ depending on the architecture of the hybrid samples, clearly indicating differences in the in-plane characteristic length scales for the different samples.^{41,56–58} Two horizontal line profiles (shown in the lower panels of images in Figure 3b–f) were extracted out of the GISAXS image at q_z (where $q_z = (2\pi)/(\lambda) \sin(\alpha_i + \alpha_f)$) values of 0.57 and 0.72 nm^{-1} . The mathematical formulation for the variation of the effective penetration depth (z) of the X-rays within the thin film as a function of exit angle (α_f) (for a fixed α_i in the GISAXS geometry) including dispersion (δ) and absorption (β) of the X-rays⁵⁷ is given by

$$z_{1/e} = -\lambda/(4\pi B(\alpha_f)) \quad (1)$$

where

$$B(\alpha_f) = \frac{1}{\sqrt{2}} \sqrt{\sqrt{(\alpha_f^2 - 2\delta)^2 + 4\beta^2} - (\alpha_f^2 - 2\delta)} \quad (2)$$

This leads to a different penetration depth of 5 and 550 nm (corresponding to q_z values of 0.57 and 0.72 nm^{-1} , respectively) to probe the in-plane correlation lengths at different thicknesses in the film.

The GISAXS images of the pure DIP and the AuNPs, which constitute the hybrids, also show clear signature of in-plane correlations (Figure 3b,c) and there is no change in the peak position for different q_z values. The interisland distances extracted from the GISAXS profiles are 350 and 286 nm for the pure DIP and pure AuNP (concentration 0.25 mg/mL) films, respectively. For the sample with AuNP at the bottom of the DIP layers (Au^{bot}), we can see two distinct correlation peaks, one corresponding to the DIP islands (real space interisland distance of 140 nm) and the other corresponding to the AuNP characteristic length scales (interisland distance of 300 nm) at two different values of q_z (see Figure 3d). This demonstrates that for such hybrid structures, the in-plane characteristic length scales depend strongly on the distribution of the respective materials along the vertical direction. In other words, the DIP length scales dominate the low q_z area, while at higher q_z values the length scales corresponding to the AuNP prevail.

We also observe that the length scale of the islands in the pure DIP film (350 nm) is different from the length scale of the DIP islands in the Au^{bot} sample (140 nm), suggesting that the AuNP at the bottom appreciably influences the island size and

distances of the DIP overlayers (compare Figure 3b,d). For the sample with Au on top of the DIP films (Au^{top}), the top surface is quite smooth (as evidenced by the low diffuse intensity in the 2D GISAXS image), but the characteristic length scale is too large to be resolved (Figure 3e) using the present experimental setup. For the sample with AuNPs sandwiched in between the DIP layers (Au^{sand}), the sample is too rough (strong diffuse scattering in the GISAXS image), and there is no resolvable in-plane peak (Figure 3f).

X-ray Reflectivity and Grazing Incidence Diffraction.

XRR is used for the extraction of the electron density profile in thin films along the direction perpendicular to the sample surface.⁵⁷ The reflected intensity is measured as a function of q_z and structural parameters like surface and interface roughness of thin films, film and layer thicknesses, and interdiffusion at the interfaces are determined. The XRR profiles of the pristine DIP and AuNP films as well as the Au^{bot} , the Au^{top} , and the Au^{sand} hybrid thin films are shown in Figure 4a. The XRR of the pure AuNP thin film gives a measure of the thickness and is about 3 nm, further confirming that the AuNP thin film is indeed only a monolayer as observed also in the AFM image in Figure 2b. The first two out-of-plane Bragg peaks of DIP observed at

~ 0.37 and $\sim 0.74 \text{ \AA}^{-1}$ in q_z for the pure DIP film clearly indicate that DIP grows mostly in the standing-up-phase (σ -phase).^{38,39} It is also observed that the presence of the AuNPs, in different layering strategies within the DIP matrix, appreciably affects the out-of-plane structure of the DIP host matrix.

For the Au^{top} sample, the XRR resembles the XRR of pure DIP but with distinctly enhanced Laue oscillations and sharper Bragg peaks indicating improved out-of-plane coherence. Here, coherence is a measure of the out-of-plane crystallite size in the thin film structure which scatter in phase. The real space value of this coherent length scale (estimated from the periodicity of the Laue oscillations) is ~ 30 nm. This is quite remarkable because the film thickness increased by more than 10 nm (nominal thickness of pure DIP film was about 20 nm) on addition of the AuNPs dispersed in toluene by spin-casting on top of the DIP. This signifies that under the influence of toluene there is some reorganization of the material in the vertical direction due to which the final thickness after restructuring as well as the out-of-plane coherence of the film increases. Such observations of enhanced crystallinity in materials, due to postdeposition exposure to the solvent (also known as solvent annealing) have been reported in several organic systems^{64–68} and have been exploited to fabricate crystalline thin films on substrates with or without a patterned structure. We shall revert to this issue later in the text (subsection: Atomic force microscopy).

However, contrary to the Au^{top} , the XRR for the Au^{bot} sample, where the DIP was grown on top of the AuNP layer, shows broader Bragg peaks and fewer Laue oscillations than the Au^{top} sample suggesting reduced out-of-plane order as well as smaller coherent crystallite size. The out-of-plane Bragg peaks of the Au^{sand} can be fitted with two Gaussian peaks (see, e.g., the 2nd Bragg peak in Figure 4a), indicating the coexistence of a weak and a strong out-of-plane order in the film from the top half and the bottom half, respectively. Since there is no change in the central peak position of the two peaks used to fit the Bragg peak, this implies that, although there is a difference in the out-of-plane order (one much weaker than the other), both peaks stem from the σ -phase of DIP. Additionally, the XRR profile does not feature any Laue oscillations as observed for the Au^{top} and the Au^{bot} samples, indicating lack of coherence in the out-of-plane direction. The XRR profiles of the samples prepared with different concentrations of the AuNPs (not shown here) also show a similar trend.

The GIXD measurements of the hybrid samples (see Figure 4b) demonstrate that the in-plane crystalline size also changes depending on the layering strategies of the AuNPs within the host DIP matrix. All the GIXD peaks observed belong to the DIP thin film phase.^{39,69} The peaks corresponding to the (1 1 0), (2 0 0), and (2 1 0) planes could be easily identified and although we scanned for higher q_{\parallel} values there was no detectable Au peak. The DIP peaks in the GIXD of the Au^{top} and Au^{sand} are similar to the pure DIP film, but those for the Au^{bot} sample are broader than the ones in the Au^{top} and the Au^{sand} samples, indicating smaller in-plane crystallite size of the DIP molecules. The crystallite sizes estimated by using the Scherrer formula are 235, 348, and $338 \text{ \AA} \pm 5\%$ for the Au^{bot} , the Au^{top} and the Au^{sand} samples, respectively.

Atomic Force Microscopy. The AFM images of the three sets of samples together with that of a pure DIP are shown in Figure 5 with the height distribution and typical line profile shown in the lower panel of the respective images. The AFM image for pure DIP (see Figure 5a) shows a typical “wedding-

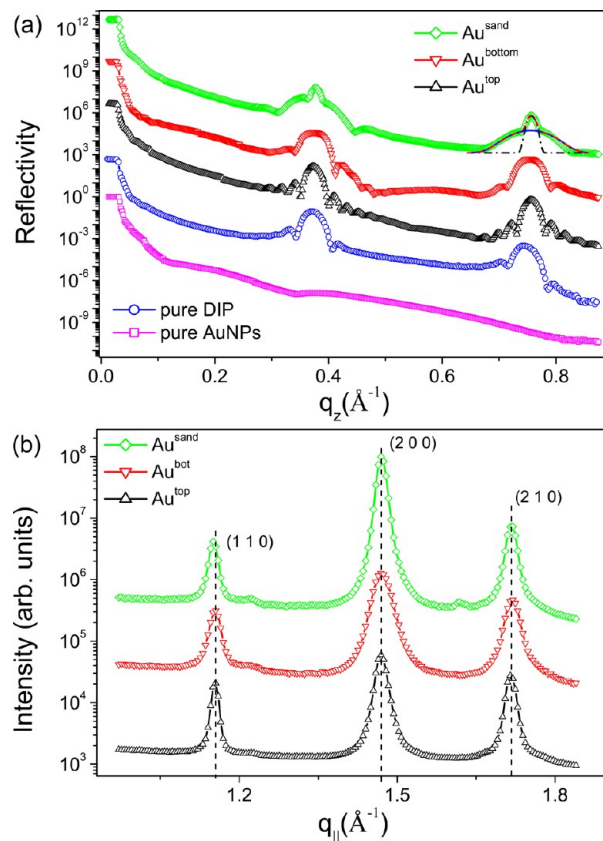


Figure 4. (a) XRR profiles for the pure DIP and pure AuNP, as well as the Au^{bot} , Au^{top} , and Au^{sand} hybrid thin films. The concentration of the AuNPs used was 0.25 mg/mL. The XRR for the Au^{sand} sample shows a superposition of two Bragg peaks arising from the two DIP layers that sandwich the AuNP layer (see fitting of 2nd Bragg peak). (b) GIXD profiles for the hybrid structures. The Au^{top} and Au^{sand} samples exhibit in-plane peaks of the thin film phase of DIP (not shown) with similar peak widths. However, the Au^{bot} sample shows much wider peaks than pure DIP. This corroborates the observation of smaller DIP islands (compared to pure DIP), which are composed of small in-plane DIP crystallites. All data have been scaled for clarity.

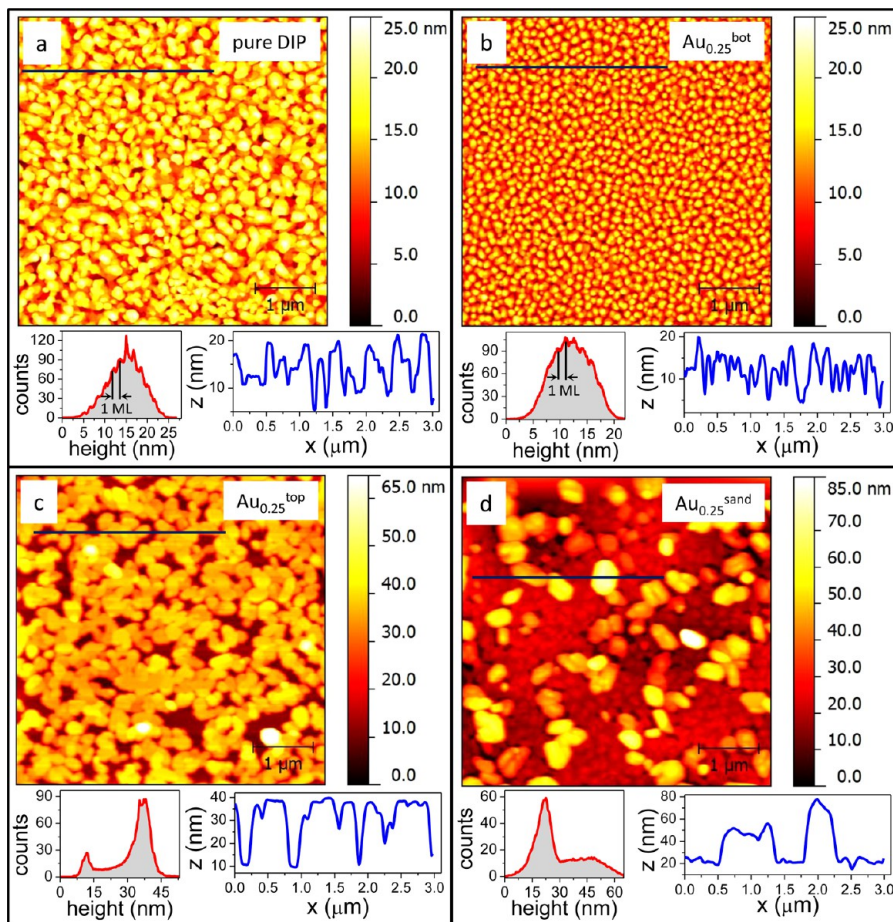


Figure 5. AFM images of (a) the pure and (b–d) the hybrid samples (0.25 mg/mL AuNP concentration) with the height distribution and typical line profile shown in lower panel of the respective images. For pure DIP (a), one sees typical “wedding-cake-like” structure with a step size of 1 monolayer (ML) of DIP, for the Au^{bot} sample (b), we observe similar “wedding-cake-like” structures, which are however smaller and more ordered than (a), for the Au^{top} sample (c), we observe that the “wedding-cake-like” islands are replaced by plateau-like islands, and finally, for the Au^{sand} sample (d), we observe that the bottom half of the sandwich layer resembles typical DIP island-like growth but the top half layer of DIP (grown over the AuNP layer) forms large 3D crystallites.

“wedding-cake-like” structure³⁸ with a thickness of ~20 nm and a step size of 1 monolayer of DIP.

For the Au^{bot} sample we observe smaller but more ordered islands when compared to pure DIP. The step size here is also the height of one monolayer of DIP. This evidence “wedding-cake-like” growth of DIP similar to pure DIP (Figure 5b) but with smaller islands having reduced crystallite size in both the out-of-plane as well as the in-plane direction. This observation was also concurred by the presence of broader (out-of-plane as well as in-plane) Bragg peaks in the XRR (Figure 4a) and GIXD (Figure 4b) measurements.

For the Au^{top} sample, as shown in Figure 5c, we observe that the typical “wedding-cake-like” islands of DIP are replaced by plateau-like coalesced islands with very smooth tops. The height profile does not show any ML step edges but rather a typical distribution of islands with similar heights on the substrate. Both the height and the line profiles show increased thickness (~30 nm) for the plateau-like islands and voids in between them. Generally, DIP grows in layer-by-layer mode for the first few monolayers and then there is a transition to 3D islanding.⁴⁰ Under the influence of the solvent, the entire film is restructured in a way such that voids are created in the film and the plateau-like islands have now an increased height (~10 nm more than the original thickness as is obvious from the

comparison of Figure 5a,c) due to redistribution of the DIP molecules from the voids. Similar restructuring was observed for DIP films spun cast with pure toluene without any dispersed nanoparticles (not shown here) to confirm the effect of the solvent. This restructuring is also evidenced by the increased out-of-plane order observed in the XRR profile (Figure 4a) although the in-plane order is mostly unaffected (Figure 4b). The morphology, however, undergoes a drastic change from typical “wedding-cake-like” island-like growth to plateau-like growth. This effect of solvent annealing is quite appreciable on the film structure and morphology of small organic molecules, which generally show poor solubility and hence have to be deposited by vacuum-based techniques. The structure of the molecules remains intact as evidenced by the presence of the out-of-plane and in-plane Bragg peaks, however, the post-deposition solvent annealing increases the mobility and diffusion of such molecules and leads to a different morphology altogether.

Finally, for the Au^{sand} sample (see Figure 5d), we observe that the bottom half layer of the sandwich structure exhibits the island-like structure of DIP but the top half layer of DIP grown over the AuNPs forms large 3D crystallites with defined edges (i.e., no layer by layer growth at all). This is also confirmed by the X-ray scattering data. We see from the XRR profile that

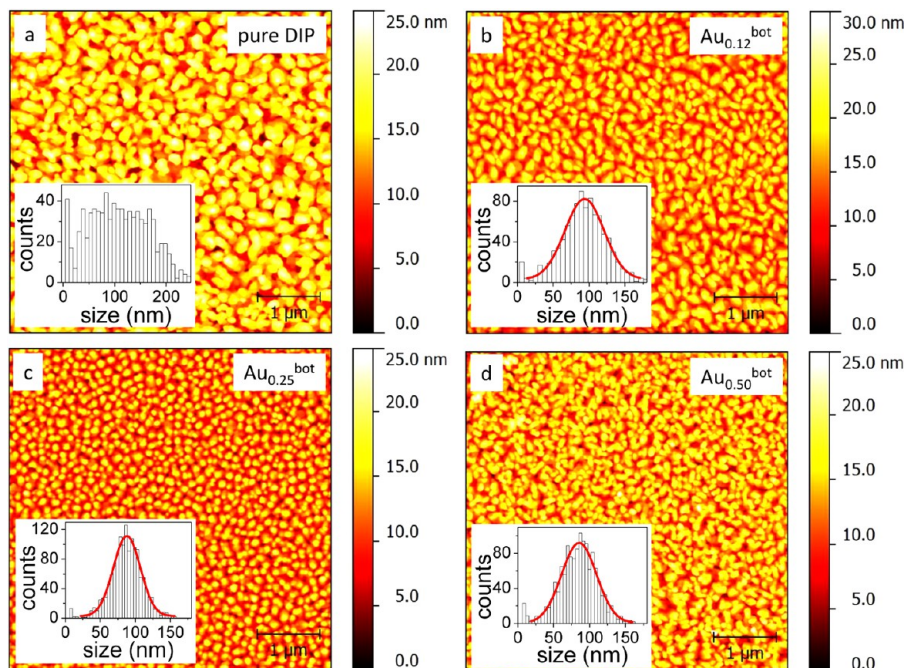


Figure 6. AFM images of the pure DIP (a) and the DIP grown on top of the different templates prepared by changing the concentration of the AuNPs from 0.12 mg/mL (b) to 0.25 mg/mL (c) and finally to 0.50 mg/mL (d). The concentration of the AuNPs changes the coverage and length scale of the ordering of the AuNPs in the template. This results in smaller islands and interisland distances of DIP. Insets show typical island-size distribution.

there exist two distinct types of out of plane order. The bottom half grows mostly well ordered with a sharp Bragg peak, while the top half grows with less order (hence broader peak) although both belong to the same σ -phase (see Figure 4a) of DIP. The length scales estimated from the horizontal line cuts of the GISAXS measurements for all the samples agree well with those obtained by AFM measurements.

Figure 6 shows AFM images together with the island-size distributions (in the insets) for pure DIP and DIP–AuNP hybrids (in the Au^{bot} strategy of layering) prepared by varying the concentration of the AuNPs dispersed in toluene. The DIP islands are smaller in size than the ones for pure DIP for the low concentration AuNPs ($\text{Au}_{0.12}^{\text{bot}}$) and continue to shrink in size for the predeposited monolayer of AuNPs with higher concentrations namely $\text{Au}_{0.25}^{\text{bot}}$ and $\text{Au}_{0.50}^{\text{bot}}$. The island size distributions are determined to be 94 ± 27 , 88 ± 19 , and 85 ± 24 nm for the $\text{Au}_{0.12}^{\text{bot}}$, $\text{Au}_{0.25}^{\text{bot}}$, and $\text{Au}_{0.50}^{\text{bot}}$ samples, respectively. This is expected since the unoccupied surface area decreases with the increase in the concentration of the AuNPs; however, the height of the DIP films grown on such templates (irrespective of the available surface area) are all around 20 nm.

It is known that the crystallinity of DIP (or also other molecular systems) is strongly dependent on the interaction with the substrate, growth conditions, and the interlayer and the intralayer diffusion of the molecules during the process of deposition.^{38–40} Increase in the diffusion of the molecules on the surface leads to larger island sizes with increased crystallinity. Under similar growth conditions on the same substrate, the change in crystallinity can be attributed to the disorder induced in the DIP layer due to the presence of the AuNPs. For the Au^{top} sample, the solvent annealing increases the crystallinity of the DIP in both the in-plane and out-of-plane direction as is obvious from the sharp peaks in the XRR and the GIXD profiles (Figure 4) as the morphology changes from “wedding-cake-like” to plateau-like islands. For the Au^{bot}

sample, the predeposited AuNPs create hindrance in the interlayer diffusion of the DIP molecules leading to smaller islands with reduced crystallinity. Finally, for the Au^{sand} sample, the topmost layer of DIP in the sandwich structure has a weaker order of crystallinity (since it grew on the AuNP layer with more disorder) than the bottom DIP layer, which has a stronger crystalline order (since it grew on the clean substrate) leading to overlapping Bragg peaks in the XRR, as shown in Figure 4a.

Transmission Electron Microscopy. TEM measurements provide conclusive evidence of the exact ordering of the AuNPs in the DIP matrix particularly since the entire film can be probed and both the DIP islands as well as the AuNPs (even when they are buried in e.g. the Au^{bot} and Au^{sand} samples) can be imaged.

For the Au^{bot} case (see Figure 7a1–a3), the presence of the AuNPs at the bottom of the DIP layer does not lead to any heterogeneous nucleation of the DIP. The patterned structure formed by the AuNPs on the substrate remains intact even upon deposition of DIP on top of it; however, the island sizes of the DIP are reduced with increasing concentration of AuNPs in the structure as also confirmed by AFM measurements shown in Figure 5b. This can be attributed to the fact that the presence of AuNPs on the substrate only hinders the intralayer diffusion processes of the DIP molecules during growth leading to smaller islands as compared to pure DIP. It has been reported that the organic molecules can grow on top of nanoparticles as long nanowires, with the nanoparticles providing the seed for growth,⁷⁰ but only after the nanoparticles have a critical size and under optimal temperature conditions. For nanoparticles with hydrophobic coating (as is the case here for dodecanethiol functionalized AuNPs), the DIP molecules do not have any preference to grow either on top of the AuNPs or on the free SiO_x surface.

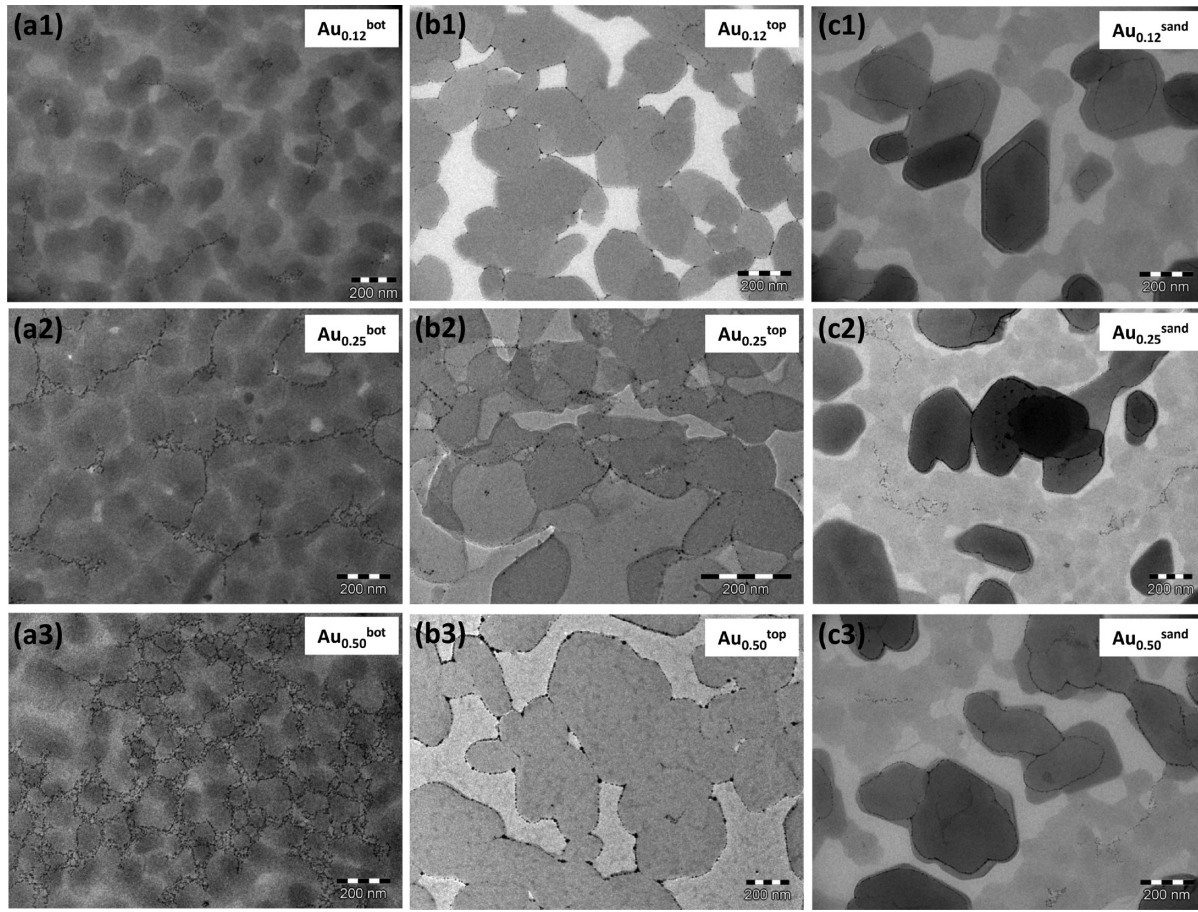


Figure 7. Representative bright field TEM images of the hybrid structures using different layering strategies. (a1–a3) Images for Au^{bot} with different concentrations of AuNPs (0.12, 0.25, and 0.50 mg/mL respectively) within the DIP matrix. We observe that the patterned structure formed by the AuNPs on the substrate remains intact even on deposition of DIP on top of it, however, the island sizes of the DIP are reduced with increasing concentration of AuNPs. (b1–b3) Typical images for the Au^{top} series (with the same concentrations of AuNPs), demonstrating that the island sizes of DIP are much larger than the ones for pure DIP and form plateau-like islands with smooth tops. Additionally, AuNPs are actually seen to be decorating the peripheral edges of the DIP islands and the number of AuNPs decorating the edges increased with the increase in the concentration. (c1–c3) Images for the Au^{sand} series, also for the same concentration of AuNPs. We clearly observe the presence of large 3D crystallites of DIP on the sandwich structure which are decorated by AuNPs. On the flat terraces of the bottom half of the DIP layer, we observe the network-like structure of AuNPs similar to the ones in the Au^{bot} sample.

For the Au^{top} sample (see Figure 7b1–b3), we observed that the island sizes of DIP were much larger than, for example, the island sizes of the pure DIP and have smooth tops, as was also confirmed by AFM measurements (Figure 5c). However, additionally we observed that the majority of AuNPs deposited on the top descended to the bottom of the DIP islands and actually positioned themselves on the peripheral edge of the islands. This decoration can be explained by the drying process.^{61,62} During late stages of drying, the remaining solvent mostly adheres to the peripheral edges of the islands and as a consequence the AuNPs are pinned and localized at the island edges. At the island corners (from where the solvent finally evaporates) there appears to be some aggregation of the AuNPs. The number of AuNPs decorating the island edge as well as the AuNP aggregates at the island corners increased with the increase in the concentration of the AuNPs. Nevertheless, with increasing AuNP concentration, few AuNPs remain on the surface of the DIP islands in the form of aggregates.

Finally, for the Au^{sand} sample (see Figure 7c1–c3), we clearly see the presence of large 3D crystallites of DIP on the top half of the sandwich structure. The bottom half resembles the

plateau-like growth of DIP islands with lateral island sizes larger than that of pure DIP film due to solvent annealing. From the TEM classical analysis we are able to observe three different ways of the AuNPs distribution on the DIP crystallites: (i) the decoration of the outer periphery of the large DIP crystallites with AuNPs; (ii) the presence of AuNPs which retain their network-like morphology; and (iii) the presence of AuNPs aggregates on the surface of DIP crystallites. The number of AuNPs decorating the island edges increases with the concentration of the AuNPs present in the sample.

For a precise location of AuNPs in this complex 3D architecture of the Au^{sand} sample, TEM tomography was used. The tomographic recording was conducted for a representative area of a sandwich architecture with a AuNP concentration of 0.50 mg/mL, Figure 8a. The analysis of the 3D reconstructed volume (see Figure 8b–d) allows us to identify precisely each layer of the complex structure from the bottom up to the top of the sandwich. Only flat terraces are observed in the bottom half of the DIP layer. For the top half layer, the slice through the 3D reconstructed volume shows the presence of DIP crystallites surrounded by AuNPs as well as the AuNP networks decorating the grain boundaries between adjacent crystallites. The AuNP

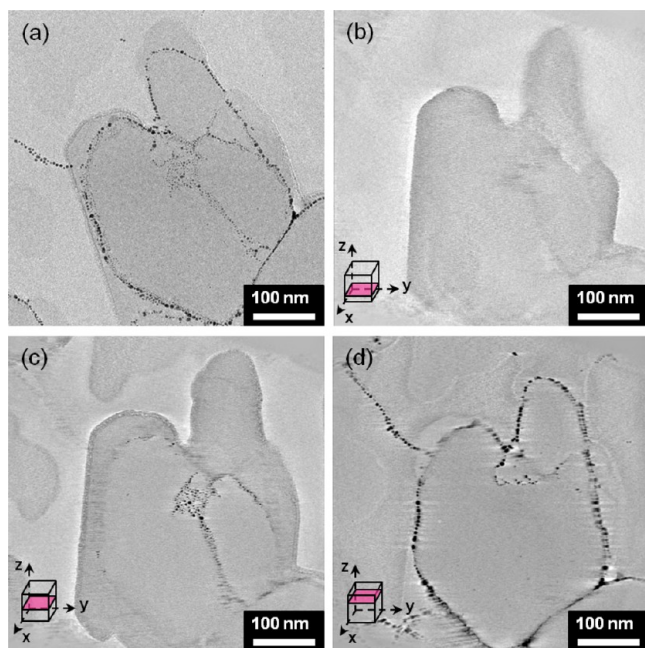


Figure 8. Tomographic analysis of a representative area of a sandwich template containing 0.5 mg/mL AuNPs: (a) given bright field 2D TEM image for 0° tilt. (b–d) Transversal slices at different depth in the 3D reconstructed volume: (b) bottom part of the sandwich structure showing a DIP crystal; (c) middle part of the film showing the contour of the underlying DIP crystal and the decorated edges of an intermediate DIP crystallite sitting atop the bottom one; (d) upper section of the film showing the top DIP crystallites fully edge-decorated by AuNPs.

aggregates are located between the two DIP layers: on the surface of the flat terraces (bottom half layer) and the grain boundaries between DIP crystallites (top half layer).

Table 1. Table Comparing the Length Scales (in nm) of the Pure and Hybrid Structures Obtained by GISAXS, XRR, GID, AFM, and TEM^a

sample	length-scale	GISAXS	XRR	GID	AFM	TEM
DIP	I_d	350 ± 30			310 ± 40	
	I_h		20.9 ± 1.1		15 ± 5	
	I_s				130 ± 60	
	I_{cs}			34 ± 1.5		
$\text{AuNP}_{0.25}$	I_d	286 ± 19			300 ± 70	300
	I_h		3 ± 0.3		3 ± 0.5	
	I_s					
	I_{cs}					
Au^{top}	I_d	unresolved			$720 \pm 80^*$	800
	I_h		29.9 ± 0.7		30 ± 4	
	I_s				$670 \pm 95^*$	
	I_{cs}			35 ± 1.7		
Au^{sand}	I_d	unresolved			$800 \pm 100^*$	700
	I_h		unresolved		50 ± 11	
	I_s				$350 \pm 30^*$	300
	I_{cs}			34 ± 2		
Au^{bot}	I_d	140 ± 21 (top), 300 ± 26 (base)			160 ± 20	200
	I_h		18 ± 1		13 ± 4	
	I_s				88 ± 19	100
	I_{cs}			24 ± 1.3		

^aThe values marked with * are not well-defined due to island coalescence. Here, I_d is the average inter-island distance, I_h is the island height, I_s is the island size, and I_{cs} is the average in-plane crystallite size.

AuNPs (at a wavelength of 520 nm) used here to enhance the local electric field in close vicinity of the AuNPs.

The PL spectra of the pure DIP and pure AuNPs, as well as the hybrid films, are shown in Figure 9. The sharp peaks

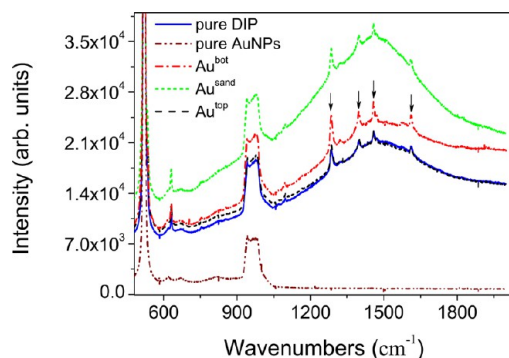


Figure 9. PL spectra of the pure DIP and pure AuNPs, as well as the hybrid films normalized to the dominant Si peak at 520 cm^{-1} . The sharp peaks (shown by arrows) present on the broad PL peak correspond to the Raman lines of DIP. The pure DIP film shows a weak PL peak around 1500 cm^{-1} , while the pure AuNP film does not show any PL in this range. We observe slight enhancement in the PL peak intensity for the Au^{bot} sample, an enhancement by a factor of 2 for the Au^{sand} sample and no enhancement at all for the Au^{top} sample.

(shown by arrows in Figure 9) superimposed on the broad PL peak correspond to the Raman lines showing different vibrational modes of DIP.^{71,72} All data were normalized with respect to the Raman peak for Si at 520 cm^{-1} for comparison. The broad feature around 960 cm^{-1} originates from the silicon substrate.⁷³ For the pure DIP sample, one observes a weak PL peak around 1500 cm^{-1} . As expected, there are no PL or Raman peaks for the AuNP thin film in this range. For the hybrid structures, we do see a change in the PL intensity pattern. A slight increment is observed in the PL peak intensity for the Au^{bot} sample. For the Au^{sand} sample, we observe an enhancement of the PL intensity by a factor of 2. However, there was no enhancement at all for the Au^{top} sample and the PL spectra almost overlaps completely with that of the pure DIP (Figure 9).

The behavior for the Au^{bot} sample can be explained by the fact that the near-field coupling will be collectively enhanced when more and more AuNPs are present near the top of the film. This is because the electric field of the impinging laser radiation decreases due to the exponentially decaying penetration depth of the radiation. Thus, there is only marginal enhancement in the Au^{bot} sample with almost all AuNPs buried at the bottom of the organic host. We do not see any enhancement in the Au^{top} sample since we have seen from AFM (Figure 5) and TEM (Figure 7) measurements that this particular hybrid structure undergoes drastic morphological reorganization under the influence of solvent. The AuNPs, though deposited on top, descend to the bottom and decorate the edges of the DIP islands and therefore essentially cannot contribute to the near-field enhancement since the electric field is exponentially reduced. For the Au^{sand} structure, however, an appreciable enhancement by a factor of 2 is observed. This can be explained by the fact that the AuNPs which should have been distributed midway in the sample, after restructuring, are now positioned on the top of the organic DIP layer as observed by TEM tomography results (Figure 8).

CONCLUSION

In conclusion, a complete structural analysis of MNP-OSC matrices has been performed. Soft incorporation of nanoparticles within OSC host matrices to induce and tune their opto-electronic properties via near-field coupling is essential for light harvesting applications since it not only ensures that the process is noninvasive, but also provides more control in the process of incorporation through tunability via the concentration, the depth inside the host matrix and the in-plane structural distribution of the MNPs. The final morphology and structure of the DIP–AuNP hybrids have been determined on the basis of X-ray scattering and AFM and TEM measurements. We have demonstrated that the different layering strategies of incorporating the nanoparticles in the host matrix lead to drastically different structures and morphologies. In particular, we have observed a remarkable increment in the out-of-plane crystalline coherence lengths of DIP upon exposure to common organic solvents which led to appreciable restructuring in the film morphology. This restructuring of the organic film also led to the complete reorganization of the AuNPs as revealed by TEM tomography measurements by identifying the exact location of the AuNPs within the organic host. The precise location of the AuNPs also explained the differences in the PL spectra measured from the DIP–AuNP hybrids with different layering strategies. Finally we have shown that AuNPs can be successfully used as tunable templates (by varying the concentration of the dispersed AuNPs in the organic solvent) for the growth of the OSCs with desired island sizes and distances. Our results provide crucial insight into the understanding of hybrid devices involving OSCs and nanoparticles.

AUTHOR INFORMATION

Corresponding Author

*E-mail: rupak.banerjee@uni-tuebingen.de.

Notes

The authors declare no competing financial interest.

ACKNOWLEDGMENTS

R.B., J.N., and M.G. acknowledge financial support by the FP7-NMP-2010-SMALL-4 Program, Project Number 263073 (HYMEC). J.N. also acknowledges support from the Project CEITEC (Grant No. CZ.1.05/1.1.00/02.0068) from the European Regional Development Fund. C.L. received financial support from the Carl-Zeiss-Stiftung. F.A. was supported by a fellowship of the University of Tübingen. M. Schmutz and C. Blank are acknowledged for technical support for TEM experiments. S.Y. acknowledges financial support from Knut and Alice Wallenberg foundation.

REFERENCES

- (1) Brütting, W.; Adachi, C., Eds. In *Physics of Organic Semiconductors*, 2nd ed.; Wiley VCH-Verlag: Weinheim, 2012.
- (2) Brabec, C. J.; Dyakonov, V.; Parisi, J.; Sariciftci, N. S., Eds. In *Organic Photovoltaics: Concepts and Applications*; Springer: Berlin; Heidelberg, 2003.
- (3) Peumans, P.; Yakimov, A.; Forrest, S. R. *J. Appl. Phys.* **2003**, 93, 3693–3723.
- (4) Forrest, S. R. *Nature* **2004**, 428, 911–918.
- (5) Forrest, S. R. *MRS Bull.* **2005**, 30, 28–32.
- (6) Atwater, H. A.; Polman, A. *Nat. Mater.* **2010**, 9, 205–213.
- (7) Linic, S.; Christopher, P.; Ingram, D. B. *Nat. Mater.* **2011**, 10, 911–921.

- (8) Liu, N.; Tang, M. L.; Hentschel, M.; Giessen, H.; Alivisatos, A. P. *Nat. Mater.* **2011**, *10*, 631–636.
- (9) Dunbar, R. B.; Pfadler, T.; Schmidt-Mende, L. *Opt. Express* **2012**, *20*, A177–A189.
- (10) Novotny, L.; van Hulst, N. *Nat. Photonics* **2011**, *5*, 83–90.
- (11) Gan, Q.; Bartoli, F. J.; Kafafi, Z. H. *Adv. Mater.* **2013**, *25*, 2385–2396.
- (12) Xie, F.-X.; Choy, W. C. H.; Wang, C. C. D.; Sha, W. E. I.; Fung, D. D. S. *Appl. Phys. Lett.* **2011**, *99*, 153304.
- (13) Yang, J.; You, J.; Chen, C.-C.; Hsu, W.-C.; Tan, H.-r.; Zhang, X. W.; Hong, Z.; Yang, Y. *ACS Nano* **2011**, *5*, 6210–6217.
- (14) Park, H. I.; Lee, S.; Lee, J. M.; Nam, S. A.; Jeon, T.; Han, S. W.; Kim, S. O. *ACS Nano* **2014**, *8*, 10305–10312.
- (15) Sung, H.; Lee, J.; Han, K.; Lee, J.-K.; Sung, J.; Kim, D.; Choi, M.; Kim, C. *Org. Electron.* **2014**, *15*, 491–499.
- (16) Gollmer, D. A.; Walter, F.; Lorch, C.; Novák, J.; Banerjee, R.; Dieterle, J.; Santoro, G.; Schreiber, F.; Kern, D. P.; Fleischer, M. *Microelectron. Eng.* **2014**, *119*, 122–126.
- (17) Derkacs, D.; Lim, S. H.; Matheu, P.; Mar, W.; Yu, E. T. *Appl. Phys. Lett.* **2006**, *89*, 093103.
- (18) Ma, L. P.; Liu, J.; Yang, Y. *Appl. Phys. Lett.* **2002**, *80*, 2997–2999.
- (19) Scott, J. C.; Bozano, L. D. *Adv. Mater.* **2007**, *19*, 1452–1463.
- (20) Chen, W.; Nikiforov, M. P.; Darling, S. B. *Energy Environ. Sci.* **2012**, *5*, 8045–8074.
- (21) Opitz, A.; Wagner, J.; Brüttling, W.; Salzmann, I.; Koch, N.; Manara, J.; Pflaum, J.; Hinderhofer, A.; Schreiber, F. *IEEE J. Sel. Top. Quantum Electron.* **2010**, *16*, 1707–1717.
- (22) Hinderhofer, A.; Schreiber, F. *ChemPhysChem* **2012**, *13*, 628–643.
- (23) Gruber, M.; Rawolle, M.; Wagner, J.; Magerl, D.; Hörmann, U.; Perlich, J.; Roth, S. V.; Opitz, A.; Schreiber, F.; Müller-Buschbaum, P.; et al. *Adv. Energy Mater.* **2013**, *3*, 1075–1083.
- (24) Karl, N. In *Organic Electronic Materials*; Farchioni, R., Gross, G., Eds.; Springer Series in Materials Science; Springer: Berlin; Heidelberg, 2001; Vol. 41; pp 283–326.
- (25) Dinelli, F.; Murgia, M.; Levy, P.; Cavallini, M.; Biscarini, F.; de Leeuw, D. M. *Phys. Rev. Lett.* **2004**, *92*, 116802.
- (26) Cicora, F.; Santato, C.; Dinelli, F.; Murgia, M.; Loi, M. A.; Biscarini, F.; Zamboni, R.; Heremans, P.; Muccini, M. *Adv. Funct. Mater.* **2005**, *15*, 375–380.
- (27) Tripathi, A. K.; Pflaum, J. *Appl. Phys. Lett.* **2006**, *89*, 082103.
- (28) Schaffer, C. J.; Palumbiny, C. M.; Niedermeier, M. A.; Jendrzejewski, C.; Santoro, G.; Roth, S. V.; Müller-Buschbaum, P. *Adv. Mater.* **2013**, *25*, 6760–6764.
- (29) Yu, S.; Santoro, G.; Sarkar, K.; Dicke, B.; Wessels, P.; Bommel, S.; Döhrmann, R.; Perlich, J.; Kuhlmann, M.; Metwalli, E.; et al. *J. Phys. Chem. Lett.* **2013**, *4*, 3170–3175.
- (30) Al-Hussein, M.; Schindler, M.; Ruderer, M. A.; Perlich, J.; Schwartzkopf, M.; Herzog, G.; Heidmann, B.; Buffet, A.; Roth, S. V.; Müller-Buschbaum, P. *Langmuir* **2013**, *29*, 2490–2497.
- (31) Fedlheim, D. L.; Foss, C. A., Eds. In *Metal Nanoparticles: Synthesis, Characterization, and Applications*; Marcel Dekker: New York, 2002.
- (32) Louis, C.; Pluchery, O., Eds. In *Gold Nanoparticles for Physics, Chemistry and Biology*; Imperial College Press: London, 2012.
- (33) Daniel, M.-C.; Astruc, D. *Chem. Rev.* **2004**, *104*, 293–346.
- (34) Jones, M. R.; Osberg, K. D.; Macfarlane, R. J.; Langille, M. R.; Mirkin, C. A. *Chem. Rev.* **2011**, *111*, 3736–3827.
- (35) Brust, M.; Kiely, C. J. *Colloids Surf., A* **2002**, *202*, 175–186.
- (36) Mangold, M. A.; Niedermeier, M. A.; Rawolle, M.; Dirks, B.; Perlich, J.; Roth, S. V.; Holleitner, A. W.; Müller-Buschbaum, P. *Phys. Status Solidi RRL* **2011**, *5*, 16–18.
- (37) Dürr, A. C.; Schreiber, F.; Münch, M.; Karl, N.; Krause, B.; Kruppa, V.; Dosch, H. *Appl. Phys. Lett.* **2002**, *81*, 2276–2278.
- (38) Dürr, A. C.; Schreiber, F.; Ritley, K. A.; Kruppa, V.; Krug, J.; Dosch, H.; Struth, B. *Phys. Rev. Lett.* **2003**, *90*, 016104.
- (39) Kowarik, S.; Gerlach, A.; Sellner, S.; Schreiber, F.; Cavalcanti, L.; Konovalov, O. *Phys. Rev. Lett.* **2006**, *96*, 125504.
- (40) Frank, C.; Novák, J.; Banerjee, R.; Gerlach, A.; Schreiber, F.; Vorobiev, A.; Kowarik, S. *Phys. Rev. B* **2014**, *90*, 045410.
- (41) Frank, C.; Banerjee, R.; Oettel, M.; Gerlach, A.; Novák, J.; Santoro, G.; Schreiber, F. *Phys. Rev. B* **2014**, *90*, 205401.
- (42) Heinemeyer, U.; Broch, K.; Hinderhofer, A.; Kytká, M.; Scholz, R.; Gerlach, A.; Schreiber, F. *Phys. Rev. Lett.* **2010**, *104*, 257401.
- (43) Kurrle, D.; Pflaum, J. *Appl. Phys. Lett.* **2008**, *92*, 133306.
- (44) Steindamm, A.; Brendel, M.; Topczak, A. K.; Pflaum, J. *Appl. Phys. Lett.* **2012**, *101*, 143302.
- (45) Topczak, A. K.; Roller, T.; Engels, B.; Brüttling, W.; Pflaum, J. *Phys. Rev. B* **2014**, *89*, 201203(R).
- (46) Wagner, J.; Gruber, M.; Hinderhofer, A.; Wilke, A.; Bröker, B.; Frisch, J.; Amsalem, P.; Vollmer, A.; Opitz, A.; Koch, N.; et al. *Adv. Funct. Mater.* **2010**, *20*, 4295–4303.
- (47) Banerjee, R.; Novák, J.; Frank, C.; Lorch, C.; Hinderhofer, A.; Gerlach, A.; Schreiber, F. *Phys. Rev. Lett.* **2013**, *110*, 185506.
- (48) Brust, M.; Walker, M.; Bethell, D.; Schiffrian, D. J.; Whyman, R. J. *Chem. Soc., Chem. Commun.* **1994**, 801–802.
- (49) Banerjee, R.; Hazra, S.; Banerjee, S.; Sanyal, M. K. *Phys. Rev. E* **2009**, *80*, 056204.
- (50) Banerjee, R.; Sanyal, M. K.; Bera, M. K.; Singh, A.; Novak, J.; Konovalov, O. *Phys. Rev. E* **2011**, *83*, 051605.
- (51) Kremer, J. R.; Mastronarde, D. N.; McIntosh, J. R. *J. Struct. Biol.* **1996**, *116*, 71–76.
- (52) Messaoudi, C.; Boudier, T.; Sorzano, C. O. S.; Marco, S. *BMC Bioinf.* **2007**, *8*, 288.
- (53) Buffet, A.; Rothkirch, A.; Döhrmann, R.; Körstgens, V.; Abul Kashem, M. M.; Perlitz, J.; Herzog, G.; Schwartzkopf, M.; Gehrke, R.; Müller-Buschbaum, P.; et al. *J. Synchrotron Rad.* **2012**, *19*, 647–653.
- (54) Santoro, G.; Buffet, A.; Döhrmann, R.; Yu, S.; Körstgens, V.; Müller-Buschbaum, P.; Gedde, U.; Hedenqvist, M.; Roth, S. V. *Rev. Sci. Instrum.* **2014**, *85*, 043901.
- (55) Nečas, D.; Klapetek, P. *Centr. Eur. J. Phys.* **2012**, *10*, 181–188.
- (56) Müller-Buschbaum, P. *Anal. Bioanal. Chem.* **2003**, *376*, 3–10.
- (57) Daillant, J.; Gibaud, A., Eds. In *X-Ray and Neutron Reflectivity: Principles and Applications*; Springer: Berlin Heidelberg, 2009.
- (58) Lazzari, R. *J. Appl. Crystallogr.* **2002**, *35*, 406–421.
- (59) Martin, C. P.; Blunt, M. O.; Pauliac-Vaujour, E.; Stannard, A.; Moriarty, P.; Vancea, I.; Thiele, U. *Phys. Rev. Lett.* **2007**, *99*, 116103.
- (60) Stannard, A.; Martin, C. P.; Pauliac-Vaujour, E.; Moriarty, P.; Thiele, U. *J. Phys. Chem. C* **2008**, *112*, 15195–15203.
- (61) Stannard, A. *J. Phys.: Condens. Matter* **2011**, *23*, 083001.
- (62) Deegan, R. D.; Bakajin, O.; Dupont, T. F.; Huber, G.; Nagel, S. R.; Witten, T. A. *Nature* **1997**, *389*, 827–829.
- (63) Roth, S. V.; Autenrieth, T.; Grübel, G.; Riekel, C.; Burghammer, M.; Hengstler, R.; Schulz, L.; Müller-Buschbaum, P. *Appl. Phys. Lett.* **2007**, *91*, 091915.
- (64) Brinkmann, M.; Wittmann, J. C.; Chaumont, C.; André, J. J. *Thin Solid Films* **1997**, *292*, 192–203.
- (65) Iwatsu, F.; Kobayashi, T.; Uyeda, N. *J. Phys. Chem.* **1980**, *84*, 3223–3230.
- (66) Mascaro, D. J.; Thompson, M. E.; Smith, H. I.; Bulović, V. *Org. Electron.* **2005**, *6*, 211–220.
- (67) Yang, J. L.; Schumann, S.; Jones, T. S. *Thin Solid Films* **2011**, *S19*, 3709–3715.
- (68) Tisserant, J.-N.; Wicht, G.; Göbel, O. F.; Bocek, E.; Bona, G.-L.; Geiger, T.; Hany, R.; Mezzenga, R.; Partel, S.; Schmid, P.; et al. *ACS Nano* **2013**, *7*, 5506–5513.
- (69) Heinrich, M. A.; Pflaum, J.; Tripathi, A. K.; Frey, W.; Steigerwald, M. L.; Siegrist, T. *J. Phys. Chem. C* **2007**, *111*, 18878–18881.
- (70) Mbenkum, B. N.; Barrena, E.; Zhang, X.; Kelsch, M.; Dosch, H. *Nano Lett.* **2006**, *6*, 2852–2855.
- (71) Zhang, D.; Horneber, A.; Mihaljević, J.; Heinemeyer, U.; Braun, K.; Schreiber, F.; Scholz, R.; Meixner, A. *J. Lumin.* **2011**, *131*, 502–505.
- (72) Scholz, R.; Gisslén, L.; Schuster, B.-E.; Casu, M. B.; Chassé, T.; Heinemeyer, U.; Schreiber, F. *J. Chem. Phys.* **2011**, *134*, 014504.

(73) Temple, P. A.; Hathaway, C. E. *Phys. Rev. B* **1973**, *7*, 3685–3697.